Mode control and mode conversion in nonlinear aluminum nitride waveguides

Matthias Stegmaier and Wolfram H.P. Pernice*

Institute of Nanotechnology (INT), Karlsruhe Institute of Technology (KIT), D-76128 Karlsruhe, Germany
**wolfram.pernice@kit.edu*

Abstract: While single-mode waveguides are commonly used in integrated photonic circuits, emerging applications in nonlinear and quantum optics rely fundamentally on interactions between modes of different order. Here we propose several methods to evaluate the modal composition of both externally and device-internally excited guided waves and discuss a technique for efficient excitation of arbitrary modes. The applicability of these methods is verified in photonic circuits based on aluminum nitride. We control modal excitation through suitably engineered grating couplers and are able to perform a detailed study of waveguide-internal second harmonic generation. Efficient and broadband power conversion between orthogonal polarizations is realized within an asymmetric directional coupler to demonstrate selective excitation of arbitrary higher-order modes. Our approach holds promise for applications in nonlinear optics and frequency up/down-mixing in a chipscale framework.

OCIS codes: (130.3120) Integrated optics devices; (130.3130) Integrated optics materials; (230.5750) Resonators; (160.6000) Semiconductor materials.

References and links

1. G. P. Agrawal, "Nonlinear fiber optics: its history and recent progress [Invited]," J. Opt. Soc. Am. B **28**(12), A1–A10 (2011).
2. A. Politi, J. Matthews, M. G. Thompson, and J. L. O'Brien, "Integrated quantum photonics," IEEE J. Sel. Top. Quantum Electron. **15**(6), 1673–1684 (2009).
3. A. Politi, M. J. Cryan, J. G. Rarity, S. Yu, and J. L. O'Brien, "Silica-on-silicon waveguide quantum circuits," Science **320**(5876), 646–649 (2008).
4. M. G. Thompson, A. Politi, J. C. F. Matthews, and J. L. O'Brien, "Integrated waveguide circuits for optical quantum computing," IET Circuits Devices Syst. **5**(2), 94–102 (2011).
5. C. Xiong, W. Pernice, K. K. Ryu, C. Schuck, K. Y. Fong, T. Palacios, and H. X. Tang, "Integrated GaN photonic circuits on silicon (100) for second harmonic generation," Opt. Express **19**(11), 10462–10470 (2011).
6. S. V. Rao, K. Moutzouris, and M. Ebrahimzadeh, "Nonlinear frequency conversion in semiconductor optical waveguides using birefringent, modal and quasi-phase-matching techniques," J. Opt. A-Pure. Appl. Opt. **6**, 569 (2004).
7. Z.-F. Bi, A. W. Rodriguez, H. Hashemi, D. Duchesne, M. Loncar, K.-M. Wang, and S. G. Johnson, "High-efficiency second-harmonic generation in doubly-resonant χ^2 microring resonators," Opt. Express **20**(7), 7526–7543 (2012).
8. J. S. Levy, M. A. Foster, A. L. Gaeta, and M. Lipson, "Harmonic generation in silicon nitride ring resonators," Opt. Express **19**(12), 11415–11421 (2011).
9. M. C. Booth, M. Atatüre, G. Di Giuseppe, B. E. A. Saleh, A. V. Sergienko, and M. C. Teich, "Counterpropagating entangled photons from a waveguide with periodic nonlinearity," Phys. Rev. A **66**(2), 023815 (2002).
10. K. Banaszek, A. B. U'ren, and I. A. Walmsley, "Generation of correlated photons in controlled spatial modes by downconversion in nonlinear waveguides," Opt. Lett. **26**(17), 1367–1369 (2001).
11. P. G. Kwiat, K. Mattle, H. Weinfurter, A. Zeilinger, A. V. Sergienko, and Y. Shih, "New high-intensity source of polarization-entangled photon pairs," Phys. Rev. Lett. **75**(24), 4337–4341 (1995).
12. J. L. O'Brien, "Optical quantum computing," Science **318**(5856), 1567–1570 (2007).
13. M. Eichenfield, J. Chan, R. M. Camacho, K. J. Vahala, and O. Painter, "Optomechanical crystals," Nature **462**(7269), 78–82 (2009).
14. T. P. M. Alegre, A. Safavi-Naeini, M. Winger, and O. Painter, "Quasi-two-dimensional optomechanical crystals with a complete phononic bandgap," Opt. Express **19**(6), 5658–5669 (2011).

#197285 - $15.00 USD Received 6 Sep 2013; revised 19 Oct 2013; accepted 22 Oct 2013; published 29 Oct 2013

15. C. Xiong, W. H. P. Pernice, X. Sun, C. Schuck, K. Y. Fong, and H. X. Tang, "Aluminum nitride as a new material for chip-scale optomechanics and nonlinear optics," New J. Phys. **14**(9), 095014 (2012).
16. W. H. P. Pernice, C. Xiong, C. Schuck, and H. X. Tang, "High-Q aluminum nitride photonic crystal nanobeam cavities," Appl. Phys. Lett. **100**(9), 091105 (2012).
17. W. H. P. Pernice, C. Xiong, C. Schuck, and H. X. Tang, "Second harmonic generation in phase matched aluminum nitride waveguides and micro-ring resonators," Appl. Phys. Lett. **100**(22), 223501 (2012).
18. P. Rath, S. Khasminskaya, C. Nebel, C. Wild, and W. H. P. Pernice, "Grating-assisted coupling to nanophotonic circuits in microcrystalline diamond thin films," Beilstein J Nanotechnol **4**, 300–305 (2013).
19. S. Ghosh, C. R. Doerr, and G. Piazza, "Aluminum nitride grating couplers," Appl. Opt. **51**(17), 3763–3767 (2012).
20. D. Taillaert, F. V. Laere, M. Ayre, W. Bogaerts, D. V. Thourhout, P. Bienstman, and R. Baets, "Grating couplers for coupling between optical fibers and nanophotonic waveguides," Jpn. J. Appl. Phys. **45**(8A), 6071–6077 (2006).
21. C.-C. Yang and W.-C. Chen, "The structures and properties of hydrogen silsesquioxane (HSQ) films produced by thermal curing," J. Mater. Chem. **12**(4), 1138–1141 (2002).
22. *Handbook of Optics* (McGraw-Hill, 1994).
23. A. Yariv and P. Yeh, *Photonics: Optical Electronics in Modern Communications* (Oxford University, 2007).
24. X. Chen, C. Li, C. K. Y. Fung, S. M. G. Lo, and H. K. Tsang, "Apodized waveguide grating couplers for efficient coupling to optical fibers," IEEE Photon. Technol. Lett. **22**(15), 1156–1158 (2010).
25. M. A. Foster, A. C. Turner, R. Salem, M. Lipson, and A. L. Gaeta, "Broad-band continuous-wave parametric wavelength conversion in silicon nanowaveguides," Opt. Express **15**(20), 12949–12958 (2007).
26. J.-M. Liu, *Photonic Devices* (Cambridge University, 2009).
27. Y. Fujii, S. Yoshida, S. Misawa, S. Maekawa, and T. Sakudo, "Nonlinear optical susceptibilities of AlN film," Appl. Phys. Lett. **31**(12), 815–816 (1977).
28. M. Stegmaier and W. H. P. Pernice, "Broadband directional coupling in aluminum nitride nanophotonic circuits," Opt. Express **21**(6), 7304–7315 (2013).
29. H. Fukuda, K. Yamada, T. Tsuchizawa, T. Watanabe, H. Shinojima, and S.-i. Itabashi, "Silicon photonic circuit with polarization diversity," Opt. Express **16**(7), 4872–4880 (2008).
30. L. Liu, Y. Ding, K. Yvind, and J. M. Hvam, "Silicon-on-insulator polarization splitting and rotating device for polarization diversity circuits," Opt. Express **19**(13), 12646–12651 (2011).
31. M. R. Watts and H. A. Haus, "Integrated mode-evolution-based polarization rotators," Opt. Lett. **30**(2), 138–140 (2005).
32. J. Zhang, M. Yu, G.-Q. Lo, and D.-L. Kwong, "Silicon-waveguide-based mode evolution polarization rotator," IEEE J. Sel. Top. Quantum Electron. **16**(1), 53–60 (2010).

1. Introduction

Integrated optical circuits offer the possibility to realize complex optical functionality in compact devices with small footprint and high reproducibility. Using established fabrication routines developed originally for the electronics industry, photonic circuits can be manufactured in a variety of materials, allowing for confining light into sub-wavelength structures and thus producing functional elements for chipscale manipulation of optical signals. By using nanophotonic waveguides difficulties with beam and modal stability often encountered in free-space optical setups can be avoided. Furthermore, the strong confinement of light in materials with high refractive index contrast enables high field intensities over long interaction lengths and thus an efficient test-bed for nonlinear optics [1]. In addition, recent realizations of integrated quantum optical experiments [2, 3] pave the way for future on-chip fundamental quantum optics studies and integrated optical quantum computation [4].

In the majority of integrated photonic circuits, single-mode waveguides are used, to provide precise control over the chosen modal propagation profile. While such waveguides are well suited for linear optical systems, emerging applications in nonlinear and quantum optics require access to different mode orders. Higher order optical modes are for example employed in modal phase-matching techniques [5] which, besides quasi-phase-matching [6] and orbital angular momentum conservation in whispering-gallery-mode cavities [7], are essential for the realization of efficient on-chip nonlinear optical processes as e.g. second-harmonic generation [8]. By exploiting modal dispersion, the fundamental mode of a pump wavelength can be phase-matched to a higher-order mode at the second harmonic, as a prerequisite for on-chip frequency conversion. Similarly, in order to achieve the inverse process of spontaneous parametric downconversion (SPDC) excitation of exactly this phase-matched higher-order mode is necessary to initiate the wavelength doubling process [9, 10].

#197285 - $15.00 USD Received 6 Sep 2013; revised 19 Oct 2013; accepted 22 Oct 2013; published 29 Oct 2013

SPDC is of particular interest for the generation of entangled photon pairs [11] in an on-chip environment and thus the realization of a full integrated non-classical light source required for integrated optical quantum computation [12]. In addition, the application of higher-order modes can also be beneficial in the framework of optomechanics where modal selection may be employed for optimizing optomechanical coupling and increasing the selectivity of the excited vibrations [13, 14].

Utilizing higher-order modes fundamentally requires good control over the modal composition of the guided light. While higher-order modes can conveniently be excited in free-space optics, the efficient excitation of a higher-order mode within an integrated waveguide is non-trivial. Therefore, developing suitable techniques for optical power transfer between arbitrary waveguide modes or between fibre and waveguide modes presents an ongoing challenge in on-chip photonics. However, due to the potentially large number of involved modes the evaluation of such techniques is not straightforward. In particular, guided light can only easily be detected and analyzed after it has been coupled out of the chip, during which parts of the modal information may be lost. This complicates the monitoring of the waveguide internal modal composition since it has to be deduced from externally detected light. Thus, methods that allow for unambiguous identification of excited higher-order modes are of fundamental interest.

Here we propose several methods to evaluate the modal composition of light guided through an integrated circuit and discuss a technique for efficient optical power transfer between arbitrary modes. The applicability of these methods is verified in aluminum nitride (AlN) based photonic circuits. Besides its piezo-electricity, electro-optical activity and a relatively high thermal conductivity [15, 16], AlN is of particular interest for integrated nonlinear optics due to a significant second-order optical non-linearity. Given the recent demonstration of SHG [17], AlN is also a promising candidate for the on-chip realization of SPDC. Furthermore, due a wide bandgap, AlN provides broadband transparency from the ultraviolet into infrared wavelengths. By sputter-deposition of AlN thin films onto oxidized silicon wafers the analogue to silicon-on-insulator substrates, in this case AlN-on-insulator or AOI, can be prepared on a waferscale, suitable for realizing large-scale photonic circuitry.

Using series of optical microring resonators we first measure the birefringent refractive index of sputter-deposited AlN, which provides the basis for accurate, simulation driven modal design. We demonstrate modal conversion between orthogonal polarizations for the same mode order as well as conversion between different mode orders in nanophotonic waveguides. Employing effective index matching in dispersion engineered waveguides we demonstrate near-unity power transfer. We develop several independent schemes for ubiquitously identifying higher-order modes excited by second-harmonic generation and find excellent agreement between measured data and numerically predicted mode orders. Our results hold promise for realizing integrated parametric downconversion, modal multiplexing and nonlinear optics in wideband semiconductors on chip.

2. Optical modes in AlN-ridge waveguides

The number of modes and the respective field profiles of an optical waveguide are determined by its specific geometry and the considered wavelength. The methods for identification of excited modes presented here for ridge waveguides are nevertheless directly transferable to other waveguide geometries since they rely on general properties, such as the effective mode indices, which can be derived from the propagation constant for any waveguide mode.

2.1 Device fabrication and experimental setup

Here, we study AOI based ridge-waveguide structures as schematically depicted in Fig. 1(a). The used wafer stack consists of a highly c-axis oriented polycrystalline AlN film of height h = 500 nm, which is sputter deposited onto a silicon substrate with a buried oxide layer of 2.0 μm thickness. Nanophotonic circuits are defined with electron-beam lithography using a *Jeol*

#197285 - $15.00 USD Received 6 Sep 2013; revised 19 Oct 2013; accepted 22 Oct 2013; published 29 Oct 2013

5300 50 kV system and Fox 15 negative tone e-beam resist (HSQ). Subsequently, the developed samples are etched in $Cl_2/SiCl_4/Ar$ inductively coupled plasma using an *Oxford 100* system. The resulting waveguide structures are connected to focusing grating couplers for out-of-plane optical access. Fabricated photonic circuits exhibit in the telecoms C-band low insertion loss down to 11 dB, corresponding to an overall transmission of up to 8%. The insertion loss consists of 5 dB input and output coupling losses and propagation loss of approximately 3.5 dB/cm, respectively. The performance of the fabricated devices is characterized using transmission measurements. For that, light is coupled in and out of the integrated circuits with focusing grating couplers, whose central coupling wavelengths are suitable adjusted to be in the required spectral regimes [18, 19]. Besides their convenience for quick and reliable measurement, these gratings benefit from being mode sensitive due to their dependence on the effective grating index [20]. Between $\lambda = 1500$ nm and $\lambda = 1630$ nm, the tunable lasers *New Focus TLB-6600* and *Santec TSL-510* are used in combination with a low-noise photodetector (*New Focus 2117*). In the measurement setup an additionally employed fibre polarization rotator enables control of the polarization of the light sent to the chip. In contrast, for measurements outside of the spectral band covered by the tunable laser sources, unpolarized light from a supercontinuum source (*Leukos SM-30-UV*) with a broad spectral output between 350 nm and 1750 nm is employed. In this case, the transmitted signal is analyzed with two spectrometers (*ANDO AQ-6315A* or *Ocean Optics JAZ*), depending on the spectral regime and the intensity of the light to detect.

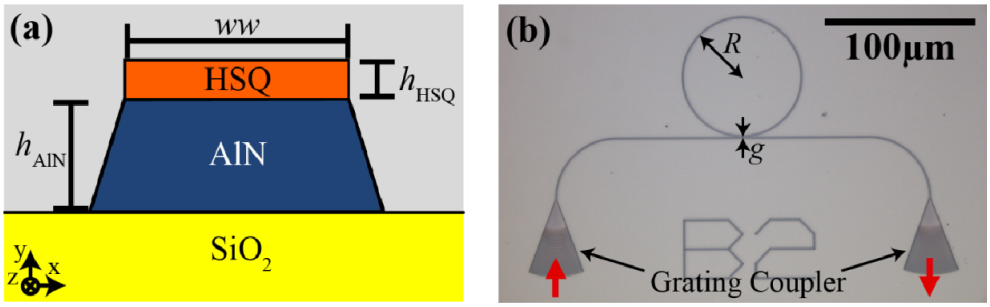

Fig. 1. (a) Basic structure of the studied AOI based ridge-type waveguides. The AlN film of height $h_{AlN} = 500$ nm is fully etched down to the underlying silica layer while the remaining e-beam resist HSQ of approximately $h_{HSQ} = 140$ nm is left on top. Resulting from the fabrication, sloped sidewalls with $\theta = 12°$ are observed. (b) Optical micrograph of a fabricated device with evanescently coupled ring resonator for evaluation of the group index from measured free spectral ranges (FSRs). Light is coupled into the structure by the grating coupler on the lower left and out by the one on the lower right. The ring resonator is separated from the waveguide of width *ww* = 650 nm by a small gap *g* = 550 nm.

2.2 Finite-element simulations

In order to design suitable AOI photonic circuits numerical simulations are performed initially. Besides their importance for the design of new devices, accurate simulations are also important for the interpretation of experimental data. In particular in case of multimode waveguides, good knowledge of the properties of the guided modes is essential, especially given the complexity of the system. Therefore, we used finite-element analysis with COMSOL® to predict the number of guided modes of the considered ridge-waveguides and their respective properties. Since different modes can exhibit similar properties, e.g. only slightly differing values of the group index n_g, accuracy of the simulation is an important issue to identify an excited mode unambiguously. Hence, the used input parameters for the FEM-simulation have to be chosen as accurate as possible. For this purpose, the geometrical quantities like width, heights and sidewall angle were extracted from high-resolution SEM-micrographs. Furthermore, fused silica is accurately described by the refractive index $n_{SiO2} = 1.444$ while in case of HSQ $n_{HSQ} = 1.4$ is adequate. Here, the exact refractive index of HSQ is

#197285 - $15.00 USD Received 6 Sep 2013; revised 19 Oct 2013; accepted 22 Oct 2013; published 29 Oct 2013

not known as it depends on various parameters like the concentration and the processing technique [21] but due to the small width of the remaining layer, deviations do not change the simulation results considerably. In contrast, the optical properties of AlN itself determine sensitively the properties of the waveguide. We expect that the used polycrystalline AlN film still exhibits birefringence like its crystalline counterpart due to its columnar micrograin structure with strong c-axis orientation. Hence, in the simulation the ordinary $n_{AlN,o}$ and extraordinary $n_{AlN,e}$ refractive indices were taken into account separately. However, these refractive indices deviate from the reported values of crystalline AlN [22] which effect cannot be neglected due to its high influence on the simulation results. Therefore, we performed series of experimental studies to derive more precise refractive index values for wavelengths around $\lambda = 1550$ nm.

2.3 Adjustment of the ordinary and extraordinary refractive index of AlN

We derive more accurate refractive indices of AlN by adjusting FEM-simulation results to experimentally measured waveguide properties. To do so, the group index is considered as it can easily be obtained from measuring the free spectral range (FSR) of evanescently coupled ring resonators [23]. In addition, the FSR can also be derived from calculated effective refractive indices. Hence, devices like the one presented in Fig. 1(b) with varying waveguide widths were studied. Here, the widths were varied to be able to adjust the refractive indices to one structure and to validate the obtained values to other geometries. For the used widths, *ww* = 450, 650 and 850 nm, the waveguide supports the fundamental TE- and TM-like mode only, cf. section 3.1. Due to their polarization, the TE-mode is almost exclusively affected by $n_{AlN,o}$ and the TM-mode by $n_{AlN,e}$ which enables studying the two refractive indices individually. The previous distinction and selective excitation of these two modes is discussed in section 3.1.

First, a resonator with waveguide width of *ww* = 650 nm and ring radius *R* = 40 µm was used to measure the group index around $\lambda = 1550$ nm. Using suitably designed grating couplers we excite both the TE- and TM-like mode in the rings to study their respective FSRs. Starting from literature values ($n_{AlN,o} = 2.12$ and $n_{AlN,e} = 2.16$ [22]) clear deviations between experiment and simulation of $\Delta n_g \approx 0.07$ (~3%) for both the TE- and TM-like mode demonstrate the requirement for more adequate values. In a next step, in the simulation the values of the ordinary and extraordinary refractive indices were varied to obtain a match with the experimentally measured results. Exemplary, the simulated dependence of the group index on $n_{AlN,e}$ is shown for the TM-like mode in Fig. 2(a). At the marked point, the calculated group index matches the experimental one. From this intersection point and the respective one for the TE-like mode, the following values could be extracted:

$$n_{AlN,o}(\lambda = 1550\text{nm}) = 2.076 \qquad n_{AlN,e}(\lambda = 1550\text{nm}) = 2.106. \tag{1}$$

Eventually, using these new parameters simulations for waveguide structures with widths *ww* = 450 nm and *ww* = 850 nm were carried out and compared to experimental values. Exemplary, in Fig. 2(b) the TM results for *ww* = 450 nm are presented. The observed good agreement demonstrates the increase in accuracy due to the adjustment of the refractive indices. Furthermore, the obtained difference between the ordinary and extraordinary value proves that birefringence is not negligible. However, despite these considerable improvements deviations between simulation and experiment due to remaining small uncertainties in both the geometrical and physical input parameters have to be expected.

#197285 - $15.00 USD Received 6 Sep 2013; revised 19 Oct 2013; accepted 22 Oct 2013; published 29 Oct 2013

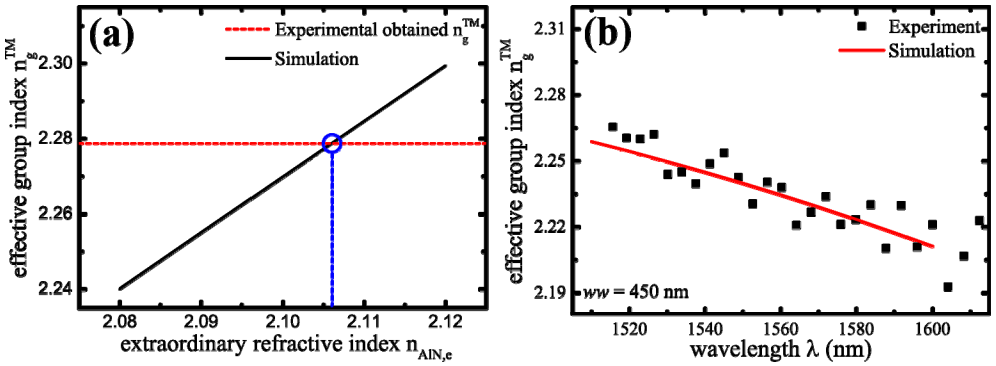

Fig. 2. Adjustment of the extraordinary refractive index $n_{AlN,e}$ of the used polycrystalline AlN at λ = 1550 nm. Due to its polarization, the TM-like mode of the ridge-type waveguide is almost exclusively affected by $n_{AlN,e}$ and can therefore be used for the respective adjustment. (a) Simulated dependence of n_g^{TM} on $n_{AlN,e}$ for a waveguide with *ww* = 650 nm. For $n_{AlN,e}$ = 2.106 the simulated value matches the measured one. (b) Comparison of measured and simulated group indices for a different waveguide geometry with *ww* = 450 nm after the adjustment of the refractive indices.

3. Experimental identification of excited modes

In a multimode waveguide it is not readily apparent by which modes a transmitted signal has been guided through the circuit. However, this knowledge is essential for achieving selective mode excitation and the analysis of circuit internal processes. For example, in cases in which the modal composition of the guided light is not altered within the waveguide structure, the respective modal components are determined by the light coupling between integrated circuit and external fibres only. Hence, identifying the modal parts of the transmitted light allows analyzing the mode selectivity of the light coupling. In contrast, various linear and nonlinear processes can lead to power transfer between different modes within the photonic circuit. In these cases, decomposing a detected signal into its modal parts can provide deeper insight into these internal processes.

The nature of an excited mode can be determined by comparing experimental accessible mode specific properties with simulation predictions. For such a distinction, the characteristic mode properties like its field profile, its specific effective refractive index or its group index can be considered. Here, the group index is most suitable since it directly affects the periodicity of all interference phenomena within the waveguide structure which can be easily observed and evaluated [23]. For example, by measuring the FSR of ring resonators or Mach-Zehnder interferometers the group index of the considered mode can be calculated and compared to simulation results. In contrast, n_{eff} can be used to predict the critical waveguide width ww_c where a specific mode is cut off [23]. By continuously decreasing *ww* this cut-off is clearly observable in the transmission spectrum since below the critical waveguide width the mode is no longer guided and therefore the corresponding transmission is strongly suppressed. Eventually, coupling characteristics in various linear and nonlinear processes can be used for mode distinction as well since they inherently depend on the mode profiles of the participating modes. For example, the coupling length L_c in directional couplers is determined by the modal overlap of the respective evanescent fields and thus varies considerably from mode to mode.

In principle, any one of these presented methods is sufficient to determine the nature of an excited mode. However, as discussed in section 2 the employed simulations depend sensitively on various geometrical and physical input parameters which suffer from small but non-negligible inaccuracies. This results in unavoidable deviations between experimental and simulation results which complicate an unambiguous identification of a mode, in particular in systems where several modes exhibit similar values of the considered property. Therefore,

#197285 - $15.00 USD Received 6 Sep 2013; revised 19 Oct 2013; accepted 22 Oct 2013; published 29 Oct 2013

several independent criteria are in general required for a clear distinction between such modes and a final identification.

In the following subsections, the discussed criteria are applied to exemplary cases of externally and internally excited modes. Since these two cases differ fundamentally in the way how the considered modes are exited they require different approaches. First, the mode excitation characteristic of the used grating couplers is studied since good control over the initial mode composition is essential for further studies of internal processes. Subsequently, second harmonic generation (SHG) in an integrated AlN circuit is discussed [17]. Here, the nature of the phase-matched mode at the 2nd harmonic is identified.

3.1 Externally excited modes by a grating coupler

As long as external light sources and detectors are used, controlled coupling of light between the integrated photonic circuits and the external fibres is of major importance for optical device characterization. Besides sufficient high coupling efficiencies, good knowledge on the mode excitation characteristic of the used technique is essential to improve device performance and analyze internal processes. Here, we use focusing grating couplers which are inherently mode sensitive [20]. In contrast to the design in [18], we use an apodized grating to suppress internal back-reflections at the coupler [24]. For that, additional 10 bars are included at the taper with linearly increasing fill factor from 75% to 85%. To study their mode excitation characteristic, simple devices like the one presented in Fig. 1(b) are used. The grating couplers are adjusted to couple light around $\lambda = 1550$ nm. In Fig. 3(a), the respective simulated geometric dispersion of the given waveguide geometry is plotted. While a singlemode waveguide is only obtained for narrow widths of 300 nm < *ww* < 400 nm, both the fundamental TE- and TM-like modes are supported for widths between 0.4 µm and 1.2 µm.

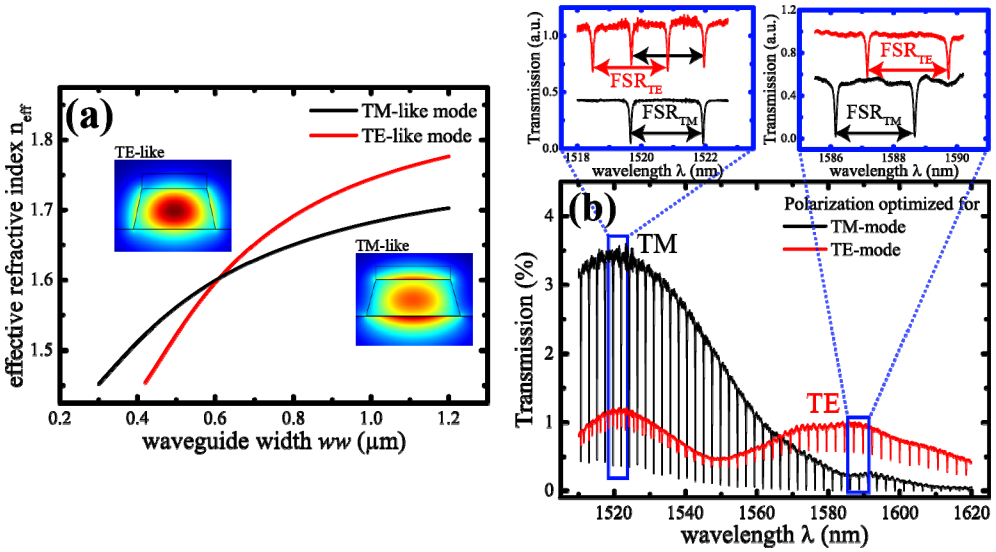

Fig. 3. (a) FEM-simulation of the geometric dispersion at $\lambda = 1550$ nm and field profiles ($|\mathbf{E}|$) of the respective guided modes. For widths *ww* between 0.4 µm and 1.2 µm, the waveguide supports the fundamental TE- and TM-like mode only. (b) Measured transmission of an apodized grating coupler for different polarizations of the incident light. Two clearly separated coupling curves corresponding to the TE- and TM- like mode are observed while the resonance peaks result from a coupled ring resonator. The excitation of different modes is confirmed by the observation of different types of resonances (different resonance wavelengths and FSRs) in dependence on the incident polarization.

#197285 - $15.00 USD Received 6 Sep 2013; revised 19 Oct 2013; accepted 22 Oct 2013; published 29 Oct 2013

Exemplary transmission curves for different polarizations of the incident fibre mode are presented in Fig. 3(b). Clearly, two separated coupling curves are observed which correspond to the excitation of the TM-like (left) and TE-like (right) mode. This assessment is supported by the fact that the respective peaks can be shifted against each other by rotating the incident polarization using the polarization controller. Additionally, this excitation of two different modes is confirmed by the observation of two types of resonances in the evanescently coupled ring resonators, cf. inset of Fig. 3(b). Around λ = 1590 nm, clearly distinct resonance wavelengths corresponding to the TE- and TM-like mode are obtained by rotating the polarization. In contrast, around λ = 1520 nm only the TE- and not the TM-resonances can be suppressed by properly adjusting the incident light. This, as well as the impossibility to suppress one of the two coupling curves completely, is most likely caused the deviations of the mode profiles from the ideal TE- and TM-cases since these make it impossible to polarize the incident light perpendicular to the waveguide modes.

After demonstrating that two different modes are coupled into the waveguides, next these modes are identified. First, the relation between observed coupling curve and excited mode is studied by looking at the respective group indices. For that, analogous to the study described in section 2.3, several ring resonator devices with different waveguide widths were fabricated. After properly adjusting the incident polarization to excite almost exclusively one mode, the corresponding group index was derived from the measured FSR. The comparison of measured values and corresponding simulation results is shown in Fig. 4(a). Due to different trends of the two modes, the already mentioned assignment of the left/right coupling curve to the TM-/TE-like mode can be made unambiguously. Besides the consistency of the trends, good agreement between simulation and experiment is achieved in case of the TE-like mode. In contrast, small deviations of $\Delta n_g \approx 0.02$ for the TM-like mode are observed which most likely result from imperfect input parameters for the simulation. However, the deviations are much smaller than the ones obtained before the adjustment of the refractive indices of AlN, cf. section 2.

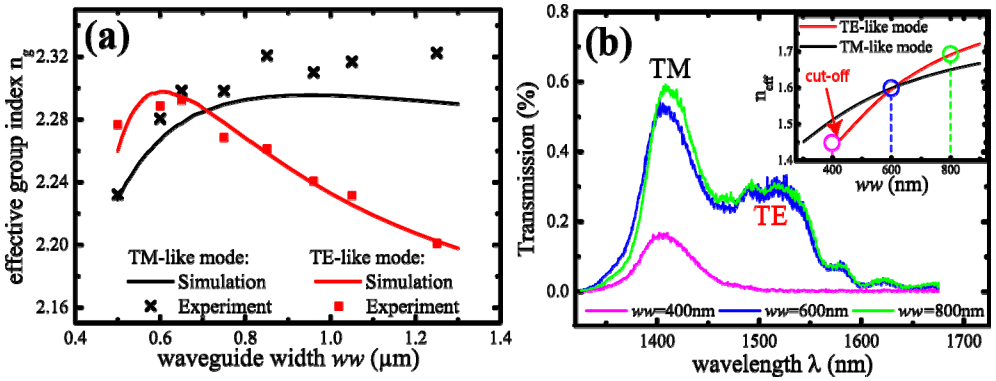

Fig. 4. (a) Comparison of measured and simulated group refractive indices at λ = 1520 nm. Due to good agreement of the observed trends, the measured modes can be related to the simulated ones. The observed small deviations are expected to result from of sub-optimal input parameters for the simulation (b) Transmission of apodized couplers for different waveguide widths. While in case of *ww* = 800 nm and *ww* = 600 nm two Gaussian shape coupling curves can be observed (TE + TM), the right one vanishes in the structure with just *ww* = 400 nm. Inset: Simulation of the geometric dispersion like in Fig. 3(a). As marked, the TE-like mode is expected to be cut-off below the critical waveguide width of ww_c = 400 nm.

Next, the cut-off waveguide widths of the guided modes are considered. According to the simulated geometric dispersion in Fig. 3(a), the TE-like mode is expected not to be guided anymore for a waveguide width below *ww* = 400 nm. This is confirmed by the measured transmission curves presented in Fig. 4(b). While at *ww* = 600 nm both the TE- and TM-like coupling curves can be observed in the transmission, the TE (right) one vanishes by going to

#197285 - $15.00 USD Received 6 Sep 2013; revised 19 Oct 2013; accepted 22 Oct 2013; published 29 Oct 2013

ww = 400 nm. The intensity decrease of the TM coupling curve is most likely caused by the fact that *ww* = 400 nm is close to the critical waveguide width of the TM-like mode as well which results in an increased propagation loss.

Both presented criteria, considering the group index and the critical waveguide width, demonstrate that the observed left/right coupling curve corresponds to the excitation of the TM-/ TE-like mode. However, in case of n_g this is only possible because the trends of the two modes differ considerably from each other. If this was not the case, the identification would not be that clear since the numerical values are not sufficient for an unambiguous classification due to uncertainties in the simulation results. In contrast, the method of considering ww_c depends fundamentally on the observation of two clearly distinct coupling curves. If these were superimposed, the suppression of one of these modes would result in a lower transmission and thus could not be clearly identified. Therefore, depending on the studied system one of these criteria or even both can be insufficient for an unambiguous identification. Due to this, it is important to have several well understood methods available.

3.2 Internally excited higher-order mode by second-harmonic generation (SHG)

Due to its significant 2nd order nonlinear susceptibility, AlN is an ideal material for integrated wavelength conversion via three-wave-mixing as e.g. SHG [15]. In case of its integrated realization, power is transferred from the originally excited mode at the fundamental frequency to a phase-matched higher-order mode at the 2nd harmonic. Hence, the modal composition is changed within the photonic circuit itself. This exemplary case of an internally excited mode differs fundamentally from the already discussed external coupling via a grating coupler in the way how the mode is excited. Thus the identification of this mode has to be tackled differently. For example, the nonlinear generation of power at the 2nd harmonic requires a precise adjustment of λ and *ww* which complicates the determination of the respective group index. Even if n_g was measured, a subsequent identification of the higher-order mode would be difficult due to the large number of guided modes and thus many similar group indices at 2ω. In contrast, here additional criteria arising from the nonlinear coupling characteristics can be employed for the mode classification.

In waveguide structures phase matching can conveniently be achieved by adjusting the waveguide width *ww* properly [25] as shown in Fig. 5(a). Here, the simulated geometric dispersion for both λ = 1550 nm and the second harmonic λ = 775 nm are plotted in the same graph. The marked intersection points correspond to the waveguide widths at which phase matching is achieved. However, deviations between these predictions and experimental conditions have to be expected due to small uncertainties in the simulation parameters. In particular, slightly deviating values of the refractive indices can lead to considerable shifts or even result in more or less phase-matching points. This complicates the identification of the internally excited higher-order mode.

However, this knowledge is essential to study and optimize the efficiency of the wavelength conversion. The actual properties of this internal process are superimposed by the characteristics of the grating couplers. Since the coupling efficiency of the grating coupler varies from mode to mode, both the nature of the involved mode at the 2nd harmonic and its coupling curve have to be known in order to deduce the actual characteristics of the SHG. In addition, as mentioned above the implementation of the reverse process of SPDC on a chip requires the selective and efficient excitation of this phase-matched mode. Hence, besides a technique for selective excitation, cf. section 4, the participating modes must be clearly known.

3.2.1 Experimental investigation of SHG in AlN

In this work SHG is realized in devices with long, meander-like shaped waveguides analogous to the ones used in [17]. Within the varied waveguide width regime ($0.8\ \mu m \leq ww \leq 1.1\ \mu m$)

#197285 - $15.00 USD Received 6 Sep 2013; revised 19 Oct 2013; accepted 22 Oct 2013; published 29 Oct 2013

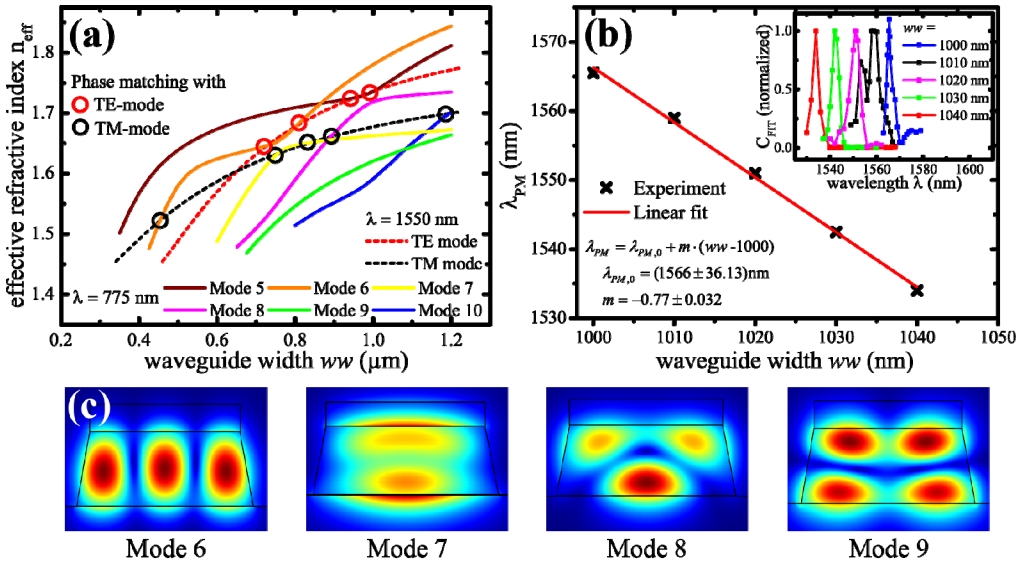

Fig. 5. (a) Calculated geometric dispersion of both the fundamental modes at λ = 1550 nm and the 2nd-harmonic modes at λ = 775 nm. The higher-order modes are numbered according to their critical waveguide widths, i.e. their first guidance while gradually increasing *ww*. Nine phase matching points are observed within the presented waveguide width regime. (b) Measured geometric dispersion of the phase matching wavelength λ_{PM} around *ww* = 1000 nm. A linear decrease is observed which represents the discussed anomalous behaviour. Inset: The respective extracted proportionalities $C_{FIT}(\lambda)$ for various devices with different waveguide widths. (c) Exemplary higher-order mode profiles ($|\mathbf{E}|$).

two phase-matching points are observed around ww = 800 nm and ww = 1000 nm. By applying different input powers at the fundamental frequency ω, the theoretically expected quadratic increase of the generated power at the second harmonic 2ω was confirmed.

$$P_{2\omega}^{wg} = \omega^2 |C|^2 \left(P_{\omega,0}^{wg}\right)^2 L^2 \sin c^2 \left(\Delta\beta L/2\right) = \overline{C}\left(P_{\omega,0}^{wg}\right)^2. \qquad (2)$$

Here, $P_{\omega,0}^{wg}$ denotes the waveguide internal power at ω, $P_{2\omega}^{wg}$ the waveguide internal generated power at 2ω, Δβ the phase-mismatch, L the length of the waveguide and C the coupling coefficient between the two participating modes. However, in the experiment not the waveguide internal powers P^{wg} but the powers P^{out} outside of the integrated circuit are measured, i.e. the contributions of the respective grating coupler efficiencies η(λ) have to be taken into account. Therefore, by plotting $P_{2\omega}^{out}$ versus $(P_{\omega,0}^{out})^2$ a straight line with the following slope is expected:

$$C_{FIT} = 2\frac{\eta_{2\omega}}{\eta_{\omega}^2}\overline{C}. \qquad (3)$$

Hence, as long as the coupling curve $\eta_{2\omega}(\lambda)$ of the higher-order mode is not known, neither the total generated power $P_{2\omega}^{wg}$ nor the coupling coefficient C can be derived.

The first step for identification of the generated higher-order mode is the controlled excitation of the TE- or TM-like mode only. Here, this is most conveniently achieved by properly adjusting the grating couplers as shown in section 3.1. In case of both observed phase-matching points, the TM-like mode was excited exclusively which reduces the number of possible modes considerably. Taking possible small deviations of the simulation into

#197285 - $15.00 USD Received 6 Sep 2013; revised 19 Oct 2013; accepted 22 Oct 2013; published 29 Oct 2013

account, in the phase-matching around *ww* = 800 nm the modes 6, 7 and 8 and around *ww* = 1000 nm the modes 7, 8 and 9 come into consideration, cf. Figure 5(a).

In the following, the nature of these two higher-order modes is studied in more detail. First, the focus is set on criteria which rely specifically on SHG. Here, the coupling coefficient which governs the strength of the nonlinear coupling and the dispersion of the phase-matching point are employed to successively exclude mode by mode. Though these considered properties are specific for SHG, the presented methods rely on properties which have similar counterparts in other circuit internal inter-mode couplings and are thus transferable. Eventually, the coupling length L_c in directional couplers is taken into account for the final identification.

3.2.2 Nonlinear coupling coefficient

Besides the phase-mismatch Δβ, the nonlinear interaction in SHG is governed by the respective coupling coefficient C which depends on a certain overlap of the participating modes and the 2nd-order nonlinear susceptibility tensor d_{AlN}. Theoretically, C can be expressed in terms of the normalized mode profiles $\boldsymbol{\mathcal{E}}_{\omega}$ and $\boldsymbol{\mathcal{E}}_{2\omega}$ and the AlN-specific form of d_{AlN} as follows [26]:

$$C = 4\varepsilon_0 \int_{\mathbb{R}^2} \boldsymbol{\mathcal{E}}_{2\omega}^{*} \cdot d\left(2\omega = \omega + \omega\right) : \boldsymbol{\mathcal{E}}_{\omega}\boldsymbol{\mathcal{E}}_{\omega} \mathrm{d}x\mathrm{d}y \equiv d_{31}C_{31} + d_{33}C_{33}. \tag{4}$$

Here, for convenience the mode overlaps C_{31} and C_{33} are defined because they are independent of the strength of the nonlinear coupling. Furthermore, it has been reported that in AlN $d_{31} \le 0.04 \cdot d_{33}$ [27] holds, i.e. the tensor-element d_{31} is much smaller than d_{33}. This is in good agreement with the observed SHG since d_{33} determines the coupling between TM-like modes. Therefore, only the interactions of the TM-like mode at λ = 1550 nm are discussed. Since it holds $C_{31} \ll C_{33}$ in cases in which a TM-like mode is involved in the coupling and $d_{31} \ll d_{33}$, the contributions of C_{31} are neglected in the following. The various values for C_{33} are derived by using the respective mode profiles obtained from COMSOL® and calculating the integral in Eq. (4) directly by numerical quadrature. The results for the still possible modes are summarized in Table 1.

In contrast, C could be experimentally derived from Eq. (3) if the coupling efficiency $\eta_{2\omega}$ was known. Even though in our case this is not directly possible, from the measured powers a lower limit of C can be estimated. In the experiment, output powers of up to $P_{2\omega}^{\mathrm{wg}} = 10\,\mathrm{nW}$ have been observed at input powers of $P_{\omega,0}^{\mathrm{out}} = 1\,\mathrm{mW}$. While the coupling efficiency at the fundamental frequency was found to be approximately $\eta_{\omega} = 0.2$, the respective efficiency of the mode at the second harmonic can be estimated upward by the maximal achieved transmission in identical reference devices, i.e. $\eta_{2\omega} \le 0.06$. By using all this and $d_{33} \approx 8\,\mathrm{pm/V}$ [27], the following lower boundary can be found: $|C_{33}|^2 \ge 10^{-8}\,\mathrm{s}^2/(\mathrm{m}^4\mathrm{A})$. Hence, by comparing the calculated values with this lower boundary it can be deduced that mode 8 and mode 9 are too weakly coupled to be one of the searched modes. Since due to the effective refractive index simulations for the SHG around *ww* = 1000 nm only the modes 7, 8 and 9 come into consideration, from this follows that here the 7th mode is excited.

#197285 - $15.00 USD Received 6 Sep 2013; revised 19 Oct 2013; accepted 22 Oct 2013; published 29 Oct 2013

Table 1. Calculated nonlinear coupling coefficients of SHG in AlN ridge-waveguide structures between the TM-mode at λ = 1550 nm and various higher-order modes at λ = 775 nm according to Eq. (4).

$\left\|C_{33}\right\|^2$ [s²/(m⁴A)]	TM-6	TM-7	TM-8	TM-9
ww = 850 nm	$1.2 \cdot 10^{-5}$	$2.43 \cdot 10^{-6}$	$2.14 \cdot 10^{-14}$	$2.24 \cdot 10^{-8}$
ww = 1050 nm	$1.25 \cdot 10^{-5}$	$1.1 \cdot 10^{-6}$	$6.45 \cdot 10^{-15}$	$3.79 \cdot 10^{-9}$

3.2.3 Geometric dispersion of the phase-matching point

Another possible criterion to identify the excited higher-order mode is the geometric dispersion of the phase matching point, i.e. how the phase matched wavelength λ_{PM} changes if the waveguide width *ww* is altered. Most conveniently, this relation is expressed in terms of its underlying properties, i.e. the wavelength dependence and geometric dispersion of the effective refractive indices. By doing so, different behaviours can instructively be explained in terms of these underlying properties and hypothetical dispersions of not phase-matched modes can be estimated. To do so, the effective refractive indices are considered as functions of λ and *ww*. Then, the respective relation can be derived by setting the total derivative $d[\Delta n_{eff}]$ of the phase mismatch between mode 1 at the fundamental frequency λ and mode 2 at the 2nd-harmonic to zero.

$$\Delta\lambda_{PM} = -\frac{\frac{\partial n_{eff}^{1}}{\partial ww}(\lambda) - \frac{\partial n_{eff}^{2}}{\partial ww}(\lambda/2)}{\frac{\partial n_{eff}^{1}}{\partial \lambda}(\lambda) - \frac{1}{2}\frac{\partial n_{eff}^{2}}{\partial (\lambda/2)}(\lambda/2)}\Delta ww. \tag{5}$$

As long as this linear approximation is valid, the slope of this relation can be predicted with COMSOL® by calculating the required derivatives with linear extrapolation. However, the absolute numbers will sensitively depend on the precise input parameter as well. Fortunately, another typical distinguishing feature can be extracted from this formula: the sign of the slope. While in general the denominator is always smaller than zero, the sign of the numerator depends on the mode combination. The former is true since the dispersion decreases rapidly with increasing wavelength. The latter can be clearly read from Fig. 5(a): while in most cases the mode at λ = 775 nm exhibits a higher slope at a phase matching point compared with the respective mode at λ = 1550 nm ("it crosses from below"), there are some cases where it is the other way around. In the first case, the dispersion of the phase matching point shows a positive slope while in the second (anomalous) case a negative slope is observed. Now, this criterion is used to confirm independently that the 7th mode is excited by the observed SHG around *ww* = 1000 nm. From the discussion above and Fig. 5(a), normal dispersion in case of mode 8 and 9 and anomalous dispersion for mode 7 are expected. Hence, from the measured anomalous dispersion presented in Fig. 5(b) it can be deduced that mode 7 is the searched mode. In addition, the experimentally measured slope m = –0.77 is in reasonable agreement with the calculated value m = - 0.55. Here, the presented phase-matching points for various waveguide widths are obtained as follows: First, the coupling coefficients $C_{FIT}(\lambda)$ are derived from linear fits of $P_{2\omega}^{out}$ versus $(P_{\omega,0}^{out})^2$. The results shown in the inset of Fig. 5(b) exhibit narrow peaks. According to Eq. (2), at the phase-matching point $\bar{C}(\lambda)$ reaches its maximal value. Since the widths of the involved coupling curves η(λ) are much broader than the nonlinear resonance, it can be assumed that at phase-matching $C_{FIT}(\lambda)$ reaches its maximum as well. Therefore, λ_{PM} is taken to be the wavelength at which $C_{FIT}(\lambda)$ reaches its maximum.

#197285 - $15.00 USD Received 6 Sep 2013; revised 19 Oct 2013; accepted 22 Oct 2013; published 29 Oct 2013

3.2.4 Coupling length L_c in co-directional couplers

In the following the focus is set on the SHG point at *ww* = 800 nm. By considering the simulated effective refractive indices and the expected coupling coefficients, the selection of the possible modes is reduced to mode 6 and mode 7. Since in accordance with the experiment in both cases an increase of $\lambda_{PM}(ww)$ is expected, this criterion cannot be used to distinguish between these modes. Therefore, another method to identify the generated mode is needed. For that purpose, photonic circuits as shown in Fig. 6(a) were fabricated to measure the coupling length within directional couplers. Light at the fundamental frequency is coupled into the circuit at the second grating coupler from the left. The subsequent Y-splitter and grating coupler on the very left are inserted as a reference for alignment. In contrast, the two output grating couplers on the right are designed to couple light around λ = 775 nm. The waveguide width *ww* before the directional coupler is suitably adjusted to achieve phase-matching. Since, however, further generation of visible light within and behind the directional coupler are not desired for the determination of L_c, the width *ww'* is increased by 30 nm. In order to perturb the system as little as possible, the transition is facilitated by a taper right in front of the directional coupler which adiabatically increases the waveguide width over a length of 100 µm. Pictures taken with the CCD-camera of devices with various interaction lengths *L* and waveguide width *ww* = 800 nm are shown in Fig. 6(b). Depending on *L*, most of the light is transferred to the upper port (L = 20 µm), is approximately split 50/50 (L = 40 µm) or exits the device at the lower port (L = 60 µm). The significant brightness decrease behind the directional coupler is a result of propagation loss. The coupling lengths L_c were now determined by evaluating several devices with varying interaction length *L* in the same way as in [28]. The results are presented in Fig. 6(c). Though the expected sinusoidal behaviour cannot be clearly seen, the results are sufficient to identify the excited mode. The obtained coupling length of 53.5 µm is in good agreement with the simulated value L_c = 50 µm of the 7th mode. In contrast, the simulated coupling length L_c = 10 µm of the 6th mode is much smaller. Therefore, this criterion clearly allows to distinguish between these two possibilities and to identify the excited mode as mode 7.

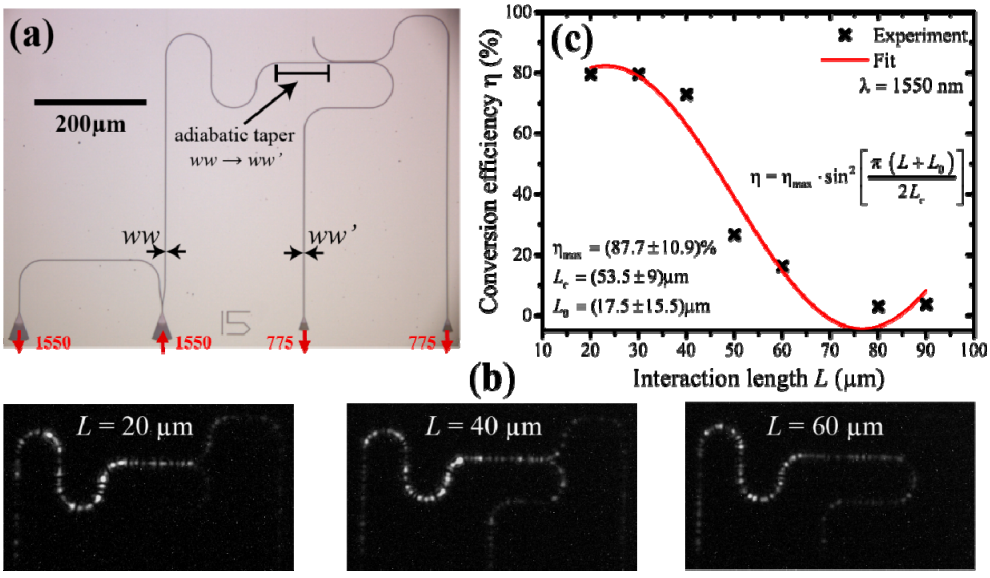

Fig. 6. (a) Optical micrograph of a photonic circuit designed for measuring the coupling length of visible light generated by SHG. While the waveguide width *ww* is designed to achieve phase matching and generate visible light, the width *ww'* = *ww* + 30 nm is chosen sufficiently off-resonance in order to prevent further SHG within and behind the directional coupler. (b) Pictures of visible scattered light for devices with different interaction lengths *L*. The pictures

#197285 - $15.00 USD Received 6 Sep 2013; revised 19 Oct 2013; accepted 22 Oct 2013; published 29 Oct 2013

were taken with a CCD-camera by using a sufficiently long integration time. (c) Measured conversion efficiencies in the directional coupler in case of the phase matching point at *ww* = 800 nm.

4. Selective excitation of guided modes

Good control over the modal composition of the coupled light is needed to study and optimize circuit internal processes which highly depend on the field profile. To achieve this, first the initial coupling of the light into the waveguide structure has to be well understood and suitably adjusted. Depending on the requirements and the coupling characteristics, this can already yield sufficient modal control. However, this is not always possible because either several modes may be excited at the same time or some modes may not be efficiently excited at all. In the first case, guiding of one specific mode can be realized by properly filtering all other modes out, e.g. via directional couplers [29]. Since this selectivity comes at the expense of reduced power, in particular for nonlinear optical applications this scheme is not suitable. Therefore, a technique for efficient power transfer from one mode to another is required to achieve highly selective excitation of a specific mode.

4.1 Concept of mode conversion in an asymmetric directional coupler

We discuss and successfully test a general method for coupling between arbitrary modes based on a co-directional structure which has also been used for polarization rotation on the SOI platform [30]. Here, using the AOI platform power conversion between the fundamental TE- and TM-like mode around $\lambda = 1550$ nm is exemplary realized due to the highly selective coupling of these modes by the used grating couplers, cf. section 3.1. Therefore, in the following the discussion is limited to this system. However, the general approach can be easily transferred to any other pair of modes in contrast to other schemes specifically designed for integrated polarization rotation [31, 32].

The geometry of the studied mode converter is schematically depicted in Fig. 7(a). It is an asymmetric co-directional structure which consists of two parallel waveguides with widths *ww* and *ww'*. Due to the small gap *g*, the evanescent fields of the single-waveguide modes overlap which leads to the desired coupling. However, power is only efficiently converted if the coupled modes are phase-matched. This is achieved by properly adjusting the waveguide widths. Considering Fig. 3(a), it can be seen that the TM-like mode at *ww* = 1060 nm exhibits the same effective refractive index as the TE-like mode at *ww'* ≈ 810 nm. Therefore, by adjusting the waveguide widths of the asymmetric structure accordingly, phase-matching between the TE- and TM-like mode is expected. This is confirmed by the simulation presented in Fig. 7(b). Here, the supermodes of the asymmetric directional coupler are analyzed. While the width of the right waveguide is left constant at *ww* = 1060 nm, the other width is varied around the expected phase-matching point of *ww'* = 810 nm. Due to the evanescent coupling between the TE- and TM-like modes, the degeneracy of n_{eff} at the phase-matching point is lifted, i.e. an anticrosssing is observed. The observed small shift of the phase matching point to a broader waveguide width *ww'* is expected to be the result of unequal self-coupling coefficients.

Though in the system at hand two unequal modes are coupled, the same relations as in the case of a symmetric directional coupler are adequate to describe the energy transfer [26]. Hence, a sinusoidal energy transfer between the TE- and TM-like modes with oscillation period $2L_c$ is expected. Here, the coupling length L_c can be calculated from the simulated phase-difference Δn_{eff} between the two supermodes [26]. At phase-matching, the simulation yields that complete power transfer is achieved at $L_{c,max} = 474$ µm. In addition, from this the maximal conversion efficiency η_{max} can be derived as follows:

$$\eta_{max}\left(\Delta n_{eff}\right) = \left(\frac{L_c\left(\Delta n_{eff}\right)}{L_{c,max}}\right)^2. \qquad (6)$$

#197285 - $15.00 USD Received 6 Sep 2013; revised 19 Oct 2013; accepted 22 Oct 2013; published 29 Oct 2013

The associated results are plotted in Fig. 7(c). A narrow resonance with a FWHM of approximately 10 nm is observed. This and the relatively high coupling length L_c result from the weakness of the interaction between the almost orthogonal TE- and TM-like modes.

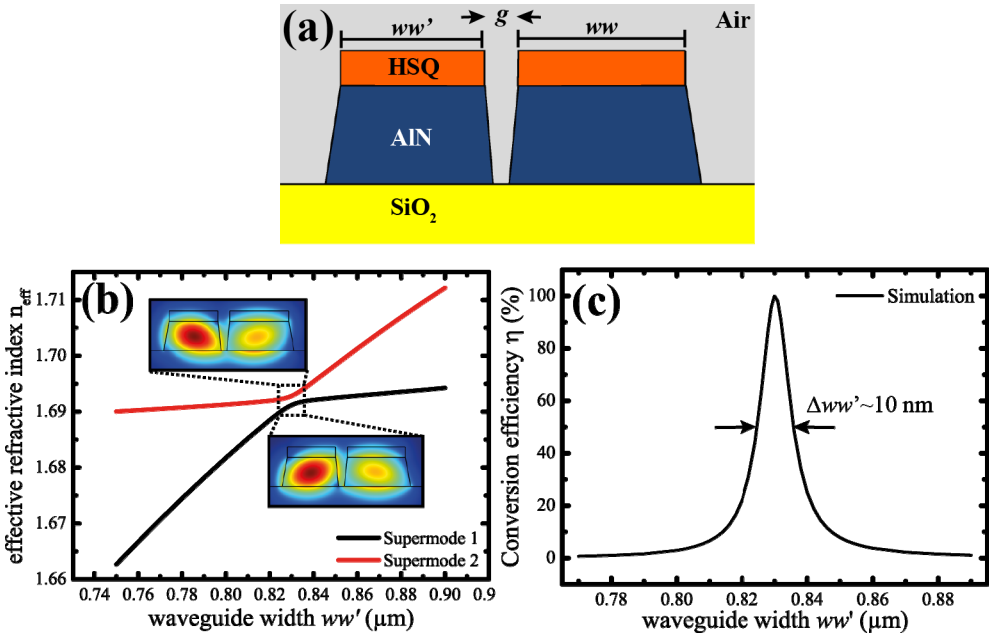

Fig. 7. (a) Cross-sectional sketch of an asymmetric co-directional waveguide structure. Two parallel waveguides with different widths *ww* and *ww'* are separated by a gap *g*. (b) Calculated geometric dispersion of an asymmetric directional coupler with a gap of 200 nm. Here, the right waveguide width was kept constant at *ww* = 1060 nm while the left one was varied. Due to the evanescent coupling, the degeneracy of n_{eff} at the phase matching point is lifted. The presented field profiles ($|(\mathbf{E})|^2$) of the supermodes at phase matching show the characteristic superposition of the coupled single-waveguide modes. (c) Calculated coupling efficiency of the studied system for various waveguide widths around the phase matching point at *ww'* = 830 nm. η was derived from the simulated geometric dispersion by using Eq. (6).

4.2 Experimental TE-TM mode conversion

An exemplary photonic circuit for the realization of a TE-TM mode converter in AlN is presented in Fig. 8(a). Note, that the photonic circuit consists of two separated parts with different waveguide widths *ww* and *ww'* which connect the ports 2/3 (lower part) and 1/4 (upper part), respectively. Here, the actual mode converter device is the asymmetric directional structure of interaction length *L* in the center. As discussed in section 3.1, the TE- and TM-like modes are coupled differently by the employed grating couplers. Most importantly, the corresponding transmission curves are well separated in wavelength from each other. On the one hand, this has to be taken into account to be able to detect any converted power. But on the other hand, this allows the clear distinction of converted TE-like and TM-like light. Therefore, the four grating couplers were designed in such a way that the ports 1/4 exhibit the TE-coupling curve at the same spectral position at which the ports 2/3 exhibit the TM-coupling curve. This is demonstrated in Fig. 8(b) where transmission measurements of identical reference couplers are summarized. Both grating couplers clearly exhibit a TE- and TM-like coupling curve, even if in case of the port 2/3 coupler the TE-like mode is much less efficiently excited as the TM-like mode. As intended, the grating coupler for port 2/3 exhibits the TM coupling curve at almost the same wavelength (λ = 1520 nm) as the grating coupler for port 1/4 exhibits the TE coupling curve. Hence, due to the overlap of the two coupling curves only TE-TM converted light could be transmitted if the two shown

#197285 - $15.00 USD Received 6 Sep 2013; revised 19 Oct 2013; accepted 22 Oct 2013; published 29 Oct 2013

grating couplers were operated in a row. In addition, a ring resonator with radius R = 50 µm is attached to port 1 to be able to measure the FSR and thus the group index of converted light. However, though measured values for converted light $T_{1\text{-}3}$ lie in the same region as values for reference TE-light $T_{4\text{-}1}$ the results scatter too much to be able to distinguish between TE- and TM-like light. This scattering is most likely caused by small power fluctuations which result from the conversion within the directional coupler.

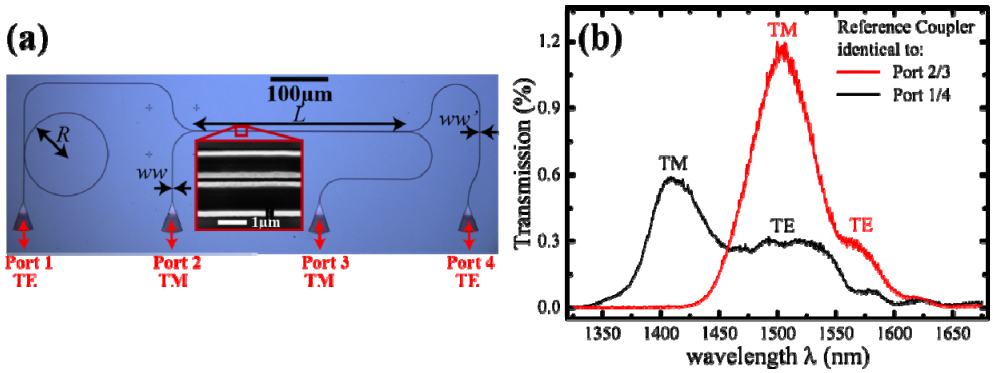

Fig. 8. (a) Optical micrograph of a photonic circuit for efficient TE-TM mode conversion. The power transfer takes place in the central asymmetric directional coupler of interaction length L if the two different waveguide widths *ww* and *ww'* are chosen properly. In order to be able to measure the mode conversion, the grating couplers 2 and 3 were designed to excite exclusively the TM-like and the grating couplers 1 and 4 the TE-like mode around λ = 1520 nm. Hence, measured signals between the ports 1/3 or 2/4 can only result from converted powers between TE and TM. (b) Measured transmission curves of two reference grating couplers identical to the ones used for the mode converter and fabricated on the same chip. Clearly, two distinct coupling curves corresponding to the TM- (left) and TE-like (right) mode (cf. section 3.1) are observed. As intended, the TE-coupling curve of the 1/4 port lies at the same position as the TM-coupling curve of the 2/3 port.

In the presented photonic circuit, four ports were used for two reasons. First of all, they allow the TE → TM and TM → TE conversion in all possible directions, i.e. $1 \leftrightarrow 3$ and $2 \leftrightarrow 4$. However, the main reason is the possibility to normalize the measured transmissions from the superimposed grating coupler curves more accurately. Though these curves are well known by studying reference couplers, the exact shape depends sensitively on the exact alignment of the external fibres above the gratings and varies slightly from device to device. Therefore, here a calibration procedure which does not suffer from these problems is used.

First, the alignment is carried out for optimal transmission $T_{1\text{-}4}$ since these ports are farthest apart and therefore are most sensitive on the precise alignment. Then, the transmissions $T_{4\text{-}1}$ and $T_{2\text{-}3}$ are recorded. Denoting the coupling efficiencies of the respective grating couplers as $\eta_{4\text{-}1}$ and $\eta_{3\text{-}2}$ and the mode conversion efficiency of the directional coupler as $\eta_{\text{TE-TM}}$, these transmissions can be expressed as follows:

$$T_{4-1} = \eta_{4-1}\left(1-\eta_{\text{TE-TM}}\right)\eta_{4-1} \qquad T_{3-2} = \eta_{3\text{-}2}(1-\eta_{\text{TM-TE}})\eta_{3\text{-}2}. \tag{7}$$

Therefore, by rearranging these two equations the ratio of coupling efficiencies can be expressed in terms of the measured transmissions:

$$\frac{\eta_{\text{TE}}}{\eta_{\text{TM}}} = \frac{\eta_{4\text{-}1}}{\eta_{3\text{-}2}} = \left(\frac{T_{4-1}}{T_{3-2}}\right)^{1/2}. \tag{8}$$

This relation proves useful in calculating the obtained mode conversion efficiency since in contrast to a symmetric directional coupler the transmitted and converted light is coupled by

#197285 - $15.00 USD Received 6 Sep 2013; revised 19 Oct 2013; accepted 22 Oct 2013; published 29 Oct 2013

two different grating couplers. Therefore, the different coupling efficiencies of the TE- and TM-like mode have to be taken into account:

$$\eta_{TM\leftrightarrow TE} = \frac{P^{wg}_{converted}}{P^{wg}_{transmitted} + P^{wg}_{converted}} = \left(1 + \frac{P^{wg}_{transmitted}}{P^{wg}_{converted}}\right)^{-1} = \left(1 + \frac{P^{out}_{transmitted}}{P^{out}_{converted}} \cdot \frac{\eta_{converted}}{\eta_{transmitted}}\right)^{-1}. \quad (9)$$

Here, P^{wg} and P^{out} denote the powers within and outside of the waveguide structure, respectively. Note that the expressions Eq. (7) and thus the determination of the coupling ratio according to Eq. (8) require an optimal polarization of the incident light which is discussed in more detail in the appendix.

In order to study the TE-TM power conversion, devices of the previously presented type with fixed ww = 1060 nm and 600 nm $\leq ww' \leq$ 900 nm were fabricated. Considerable power conversion is only observed at waveguide widths around ww' = 780 nm, where mode conversion with an efficiency of up to 75% within an interaction length of L = 360 µm was achieved. To demonstrate the observed power transfer, in Fig. 9(a) and 9(b) measured transmissions $T_{3\text{-}2}$ and $T_{3\text{-}1}$ for various interaction lengths L are shown. It can be observed that the transmitted TM power $P_{3\text{-}2}$ decreases drastically from a small interaction length of 40 µm to L = 360 µm where almost no TM-power is transmitted anymore. At the same time, the measured TE-power at port 3 increases with increasing interaction length. Hence, if the interaction length L is increased from 40 µm to 360 µm more and more power is converted from the TM-like to the TE-like mode. Note, that the sum of transmitted TM and TE power decreases considerably with L which is mainly a result of the fact that the coupling efficiency η_{TE} of port 1 is much smaller than η_{TM} of port 2.

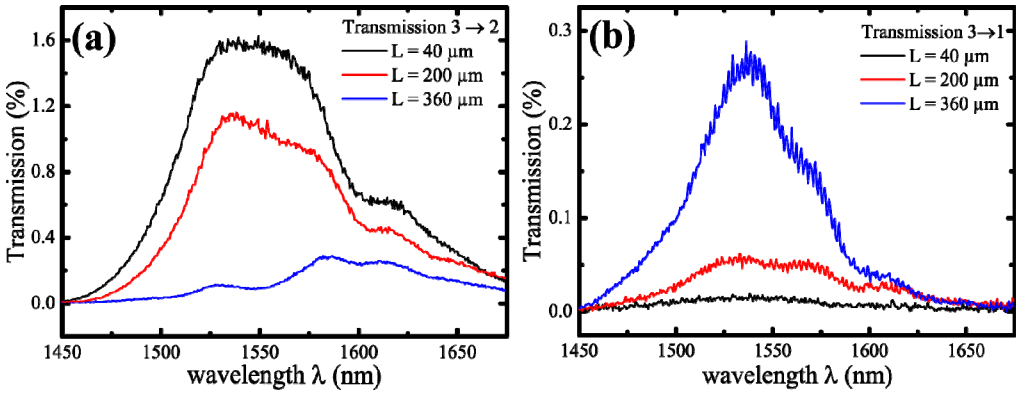

Fig. 9. Experimental results for mode converter devices with phase-matched waveguide width ww' = 780 nm. The measurements were carried out with the white light source. (a) The TM-like light in $T_{3\rightarrow 2}$ decreases gradually with increasing interaction length L until almost no power is transmitted anymore at L = 360 µm (b) With increasing L, more and more TE-like light is measured at port 1 which indicates that more and more power is converted.

The resulting conversion efficiency, calculated with Eq. (9) and Eq. (10), is presented in Fig. 10. Here, the presented TE-TM power conversion exhibits efficiencies exceeding 70% and 50% within bandwidths of 30 nm and 120 nm, respectively. Furthermore, the highest conversion efficiency of $(75 \pm 5.4)\%$ is achieved at λ = 1540 nm. In this derivation, the most dominant error source is the implicit assumption that equally designed grating couplers exhibit the same coupling characteristics. Due to slightly different grating coupler/ fibre alignments and fabrication variations, this is not perfectly true. To estimate this error, we derived the conversion efficiencies $\eta_{1\text{-}3}$, $\eta_{4\text{-}2}$ (TE → TM) and $\eta_{2\text{-}4}$, $\eta_{3\text{-}1}$ (TM → TE). Averaging the respective efficiencies yields an average error of 5.1% within the presented wavelength interval with maximal error of 7.6% at $\lambda \approx$ 1560 nm.

#197285 - $15.00 USD Received 6 Sep 2013; revised 19 Oct 2013; accepted 22 Oct 2013; published 29 Oct 2013

The observed phase-matched waveguide width ww' = 780 nm is in good agreement with the simulated value of ww' = 830 nm. In contrast, the obtained interaction length L = 360 µm deviates clearly from the expected coupling length L_c = 474 µm. This results from the fact that the almost orthogonal TE- and TM-like modes deviate from the ideal TE- and TM-polarization only in the vicinity of the waveguide boundary and in particular its edges. Therefore, the coupling is governed by the profile overlaps in these regions and is thus sensitive on the actual surface morphology which is not adequately mapped by the used simple geometry in Fig. 7(a).

Though an initial increase of converted power with increasing interaction length L is obtained, the expected characteristic sinusoidal behaviour of the power conversion is not observed. Most certainly, this results from the weakness and thus an increased sensitivity on perturbations of the coupling. As presented in Fig. 7(c), the predicted resonance with a FWHM of approximately 10 nm is quite narrow. Hence, random fluctuations as due to surface roughness of the waveguide width ww of a few nanometer are comparable to the width of the resonance and are thus most likely affecting the functionality of the studied devices. Additionally, deviations from coupled mode theory due to the small gap g = 200 nm required for efficient coupling will also contribute. In particular, this strong perturbation to the single-waveguide modes causes enhanced coupling to radiation modes and thus additional loss. In order to estimate this loss, the transmissions $T_{1\text{-}4}$ and $T_{2\text{-}3}$ were recorded in several devices with varying interaction length L and with waveguide widths ww = 680 nm sufficiently off-resonance. Plotting the obtained transmissions logarithmically versus L, a linear decrease is observed. From linear fits, coupling losses of 2 dB/mm and 4.5 dB/mm for the thick and the thin waveguide are obtained, respectively.

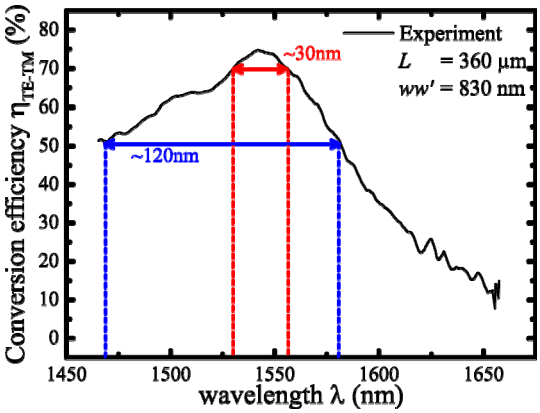

Fig. 10. TE-TM conversion efficiencies derived from the measured data, Eq. (9) and Eq. (10). Over a bandwidth of 30 nm and 120 nm, conversion efficiencies of over 70% and 50% are achieved, respectively. For clarity, error bars (average variance of 5.1% within the shown wavelength interval) are suppressed.

4.3 Discussion

In summary, the presented design allows efficient polarization rotation within a reasonable short distance of 360 µm. At the same time, the observed coupling loss of approximately 0.7 dB and 1.6 dB do not limit the application of the device in more complicated photonic circuits. In addition, due to the wide bandgap of AlN the discussed scheme is not restricted to the infrared regime as previous achievements in SOI. Furthermore, due to its electro-optical activity the design allows for active control over the converted power as well. Besides modulation of the signal, this potentially enables additional fine-tuning to achieve phase-matching. However, deviations of the power transfer characteristic from theoretical predictions indicate that a further reduction of waveguide width fluctuations is required to achieve higher control over the polarization conversion.

#197285 - $15.00 USD Received 6 Sep 2013; revised 19 Oct 2013; accepted 22 Oct 2013; published 29 Oct 2013

Most importantly in the context of this work, the design can be transferred to the conversion between arbitrary modes. Here, the interaction can be much stronger if the two coupled modes are not orthogonally polarized. Hence, in such cases less sensitivity on geometric fluctuations, higher control of the transfer characteristics and shorter coupling lengths L_c are expected.

5. Conclusions

In this work we have provided a detailed study of how the modal composition of guided waves in integrated multimode waveguides can be analyzed and controlled using aluminum nitride based nanophotonic circuits. Relying on optical resonances in integrated ring cavities, we derived experimental values for the anisotropic refractive indices of the used polycrystalline AlN film. This enables us to perform accurate simulations of the integrated structures which are essential for the identification of excited modes and the design of functional devices. We have proposed several methods to analyze the modal composition of integrated guided waves and applied them successfully to study the TE-/TM- excitation characteristics of the employed focusing grating couplers. Furthermore, we have demonstrated that the presented criteria also allow for studies of circuit-internal processes which involve interactions of various modes. Exemplary, we identified the higher-order mode excited in observed SHGs which is of interest for a future on-chip implementation of SPDC. In addition, we discussed the excitation of an arbitrary waveguide mode in an asymmetric direction coupler. In such a structure, we achieve up to 75% polarization conversion and a 3 dB-bandwidth of over 120 nm. This demonstrates the applicability of the device for efficient power conversion and thus excitation of an arbitrary mode.

Using the approaches described above we have gained sufficient control to efficiently and selectively excite either the TE- or TM-like mode. In combination with the discussed mode converter, this enables the reversible transfer of high powers into any required waveguide mode. Furthermore, choosing an adequate pair of coupled modes potentially reduces the coupling length considerably, allowing for both efficient and compact power transfer. In addition, in AlN active control over the power transfer via the Pockels effect enables both modulation and fine-tuning for phase-matching. Due to its wide bandgap, the presented schemes can straightforwardly be transferred to applications in the visible regime. Taking all together, we pave the way towards the on-chip realization of SPDC where the correctly phase-matched higher-order mode at the second harmonic has to be efficiently excited to initiate the frequency doubling. Potential applications of our work include integrated nonlinear optics, optomechanics and frequency up/down-mixing in a chipscale framework.

The expressions Eq. (7) and thus the determination of the coupling ratio according to Eq. (8) require an optimal polarization of the incident light. This can be understood in terms of Fig. 3(b) where the dependence of the overall transmission T on this polarization is demonstrated. Due to this and the fact that the coupling at the output does not depend on the input light, it is clear that the coupling efficiencies of the input and output grating coupler are in general not the same. Therefore, the coupling efficiencies η_{TE} and η_{TM} are conveniently defined with respect to accordingly polarized light because in this case holds $\eta_{input} = \eta_{output}$. Then, the input coupling efficiency is given by η_{TE}/η_{TM} times the ratio of suitably polarized light. Hence, in general Eq. (7) and Eq. (8) have to be corrected by these polarization dependent factors.

If a linearly polarized light source and a fibre polarization rotator are used, the incident light can be suitably adjusted and this problem does not arise. Here, however, we use the unpolarized white light source due to its broader spectral output. Fortunately, the problem that these factors are not known can be circumvented by measuring both the mode conversion efficiency from TE-like to TM-like mode and vice versa. Resulting from theory [26], at phase-matching these two efficiencies are expected to be the same, i.e. $\eta_{TE\text{-}TM} = \eta_{TM\text{-}TE}$. In addition, according to (9) they depend differently on the ratio of coupling efficiency and thus

#197285 - $15.00 USD Received 6 Sep 2013; revised 19 Oct 2013; accepted 22 Oct 2013; published 29 Oct 2013

on the polarization dependent factors. Hence, these relations can be used to derive the dependence of the actual mode conversion efficiency $\eta_{TE\leftrightarrow TM}$ on the measured efficiencies $\eta_{TE\text{-}TM}$ and $\eta_{TM\text{-}TE}$:

$$\eta_{TM\leftrightarrow TE} = \left(1 + \sqrt{\frac{\left(1-\eta_{TM\to TE}^{measured}\right)\left(1-\eta_{TE\to TM}^{measured}\right)}{\eta_{TM\to TE}^{measured}\,\eta_{TM\to TE}^{measured}}} \right)^{-1} . \quad (10)$$

Acknowledgments

W.H.P. Pernice acknowledges support by DFG grants PE 1832/1-1 and PE 1832/1-2. We also acknowledge support by the Deutsche Forschungsgemeinschaft (DFG) and the State of Baden-Württemberg through the DFG-Center for Functional Nanostructures (CFN) within subproject A6.4. The authors further wish to thank Silvia Diewald for assistance in device fabrication. We acknowledge support by the Deutsche Forschungsgemeinschaft and Open Access Publishing Fund of Karlsruhe Institute of Technology.